Precision solid synthesis of CoFe@FeO_x nanoparticles for regulating Li/Na–S batteries

Yanping Chen[1,#], Yu Yao[2,#], Wantong Zhao[3], Lifeng Wang[2], Haitao Li[1], Jiangwei Zhang[5], Baojun Wang[3], Yi Jia[7], Riguang Zhang[3,], Yan Yu[2,*], Jian Liu[1,4,5,6,*].*

[1] State Key Laboratory of Catalysis, Dalian Institute of Chemical Physics, Chinese Academy of Sciences, Dalian, Liaoning 116023, China.

[2] Hefei National Research Center for Physical Sciences at the Microscale, Department of Materials Science and Engineering, National Synchrotron Radiation Laboratory, CAS Key Laboratory of Materials for Energy Conversion, University of Science and Technology of China, Hefei, Anhui 230026, China. E-mail: yanyumse@ustc.edu.cn

[3] State Key Laboratory of Clean and Efficient Coal Utilization, College of Chemical Engineering and Technology, Taiyuan University of Technology, Taiyuan, Shanxi 030024, China. E-mail: zhangriguang@tyut.edu.cn

[4] DICP-Surrey Joint Centre for Future Materials, Department of Chemical and Process Engineering, and Advanced Technology Institute, University of Surrey, Guildford, Surrey GU2 7XH, UK. E-mail: jian.liu@surrey.ac.uk

[5] Science Center of Energy Material and Chemistry, College of Chemistry and Chemical Engineering, Inner Mongolia University, Hohhot 010021, China.

[6] Center of Materials Science and Optoelectronics Engineering, University of Chinese Academy of Sciences Beijing 100049, China.

[7] Department of Applied Chemistry and Zhejiang Carbon Neutral Innovation Institute, Zhejiang University of Technology, Hangzhou 310032, China

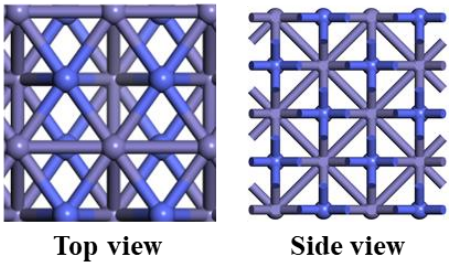

Figure S1 The side and top views of CoFe (110) surface.

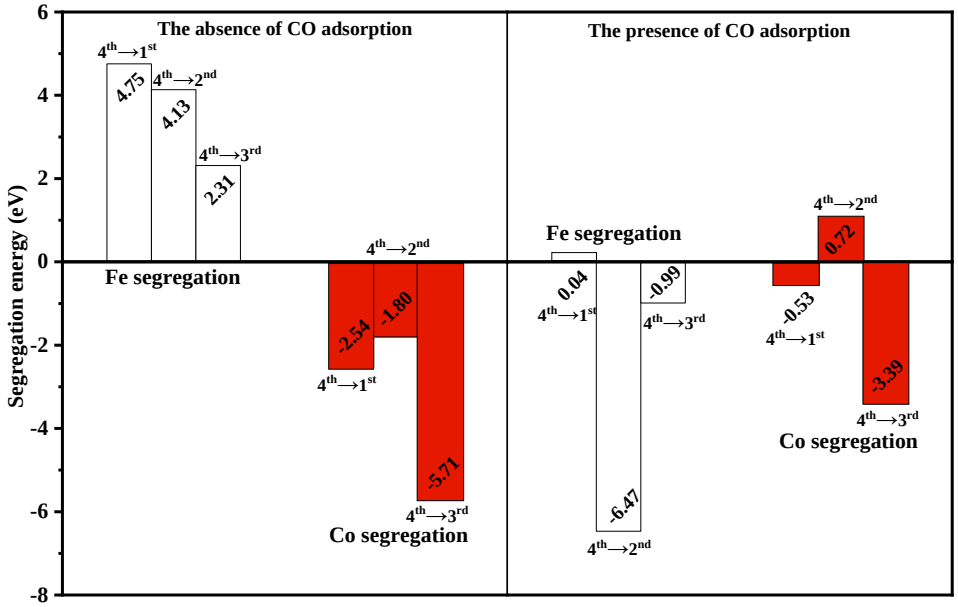

Figure S2 The segregation energy of Fe and Co atoms for the CoFe alloy in the absence and presence of CO adsorption, and the corresponding structures are presented in Figure S3.

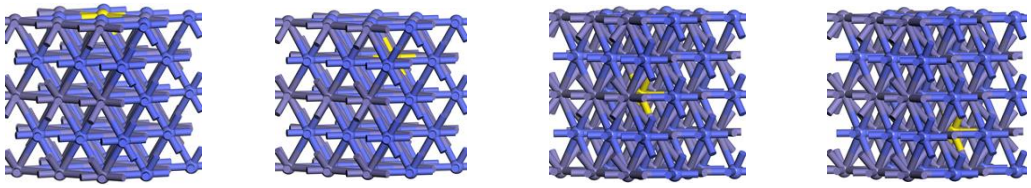

Fe located in the 1st layer | Fe located in the 2nd layer | Fe located in the 3rd layer | Fe located in the 4th layer

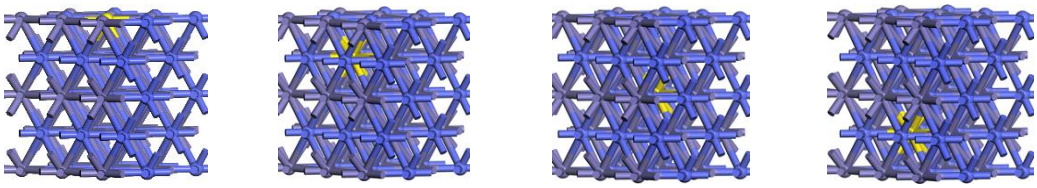

Co located in the 1st layer | Co located in the 2nd layer | Co located in the 3rd layer | Co located in the 4th layer

CoFe alloy without CO adsorption

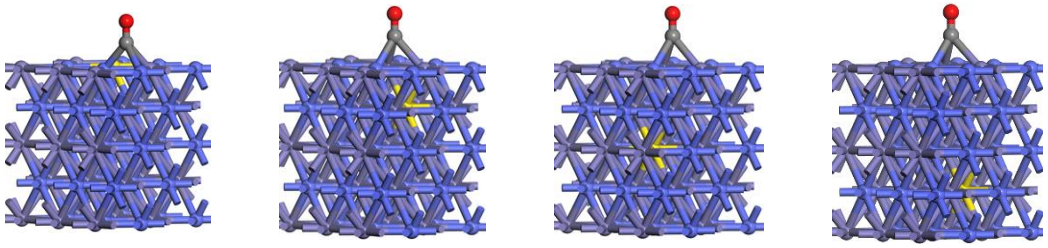

Fe located in the 1st layer | Fe located in the 2nd layer | Fe located in the 3rd layer | Fe located in the 4th layer

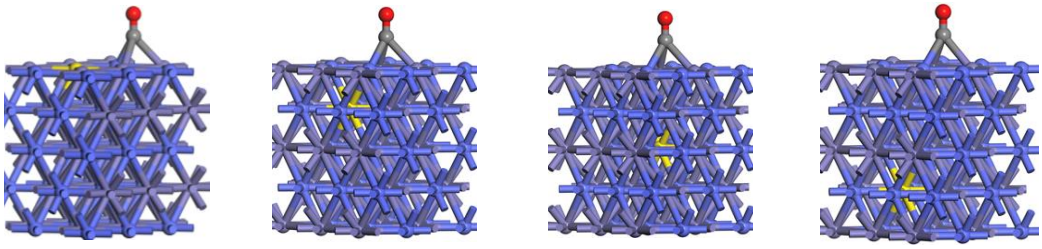

Co located in the 1st layer | Co located in the 2nd layer | Co located in the 3rd layer | Co located in the 4th layer

CoFe alloy with CO adsorption

Figure S3 The structures of Fe and Co atoms segregation for the CoFe alloy in the absence and presence of CO adsorption. The blue and purple represent Co and Fe atoms, respectively. The bright yellow represents the Fe or Co atom located in the n^{th} layer.

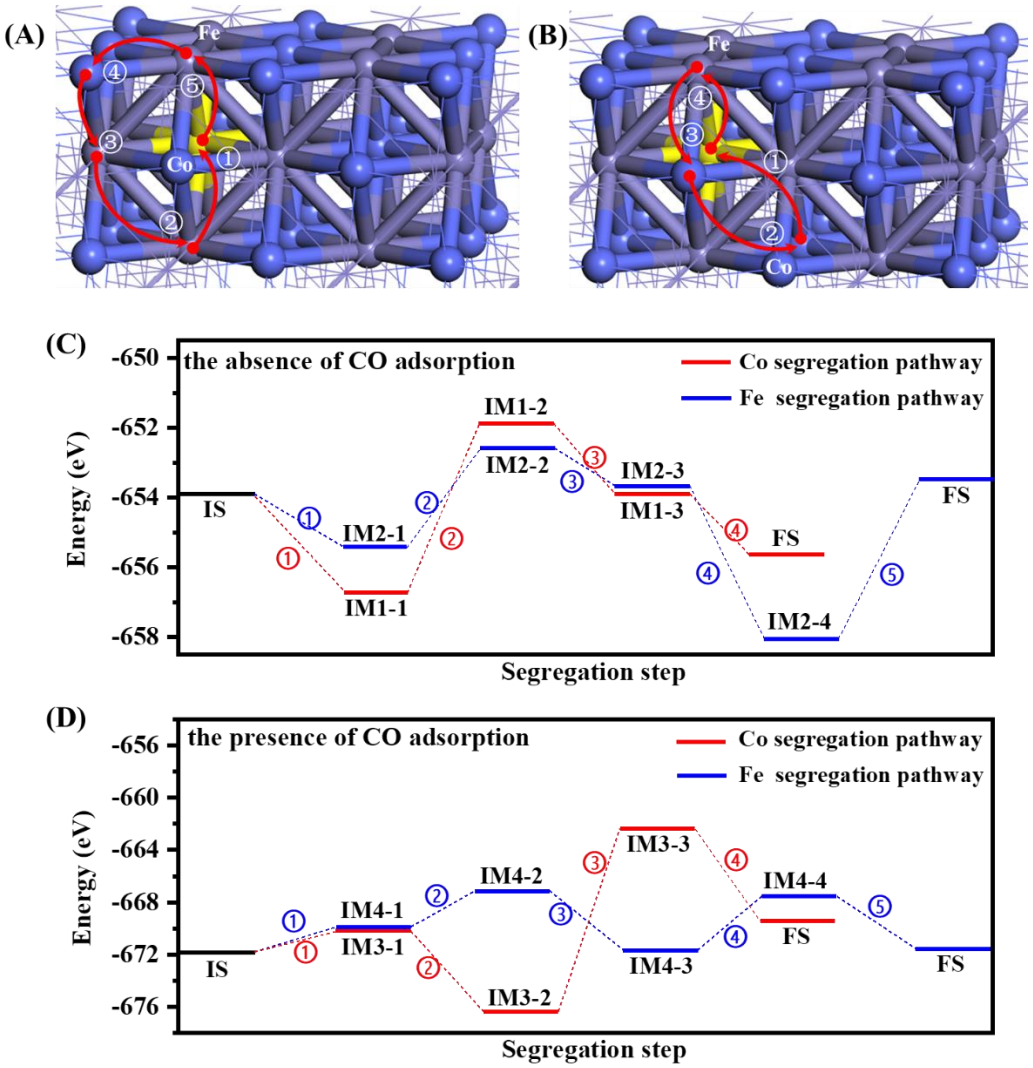

Figure S4 The segregation pathway of Fe atom (A) and Co atom (B) in the CoFe alloy with the Co vacancy located in the 2nd layer. The reaction energy profile of the Fe or Co atom segregation pathway in the absence of CO adsorption (C). The reaction energy profile of the Fe or Co atom segregation pathway in the presence of CO adsorption (D). IS, IM and FS represent the initial, intermediate, and final state, respectively. And the corresponding structures are presented in Figure S5.

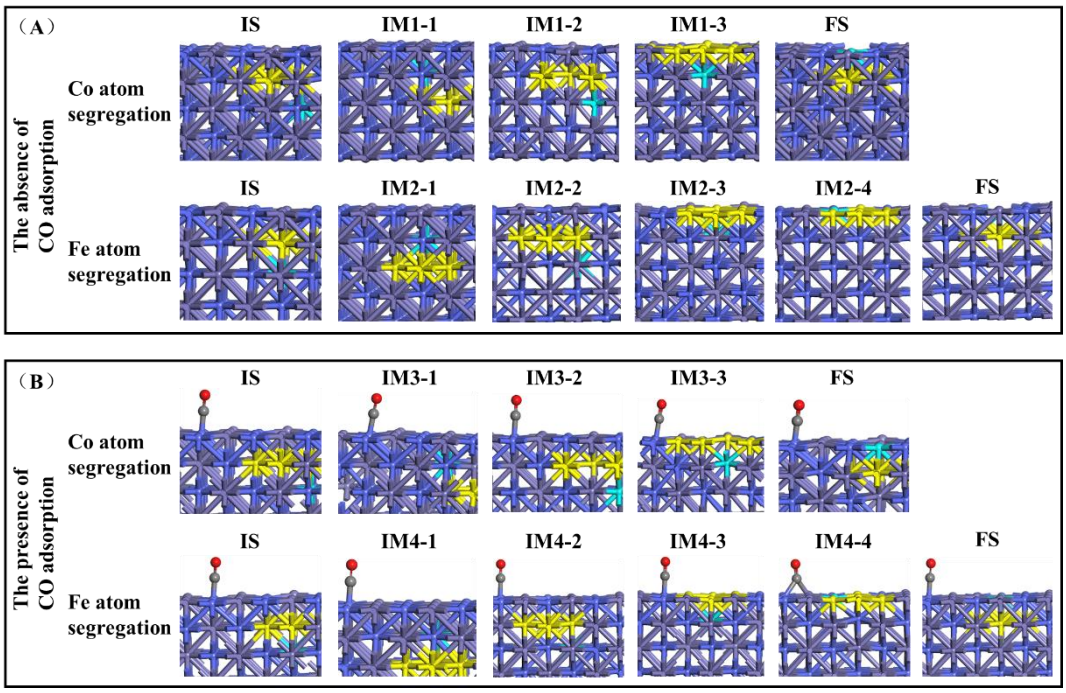

Figure S5 The structures of Fe and Co atoms segregation pathway in the absence (A) or presence (B) of CO adsorption in the CoFe alloy with Co vacancy located in the 2nd layer. IS, IM and FS represent the initial, intermediate, and final state, respectively. The blue and purple represent Co and Fe atoms, respectively. The bright yellow represents the vacancy located in the *n*th layer. The bright blue represents the M (M=Fe or Co atom) located in the *n*th layer.

For Fe atoms segregation in the CoFe alloy, as shown in Figures S2 and S3, in the absence of CO adsorption, the E_{seg-1}, E_{seg-2} and E_{seg-3} of Fe atom for CoFe alloy are 4.75, 4.13 and 2.31 eV, respectively, suggesting that the ability of Fe atom segregation from the bulk to the surface is weaker. Meanwhile, the E_{seg-1}, E_{seg-2} and E_{seg-3} of Co atom for CoFe alloy are -2.54, -1.80 and -5.71 eV, respectively, which means that the Co atom segregation from the bulk to the surface for CoFe alloy is much easier compared to the Fe atom segregation in the absence of CO adsorption. In the presence of CO adsorption, CO adsorption alters the $E_{seg-n(n=1-3)}$ of Fe and Co atoms for CoFe alloy. The E_{seg-1}, E_{seg-2} and E_{seg-3} of Fe atom are 0.04, -6.47 and -0.99 eV, respectively, indicating that the Fe atom segregation from the bulk to the surface easily occurs. However, for Co atom segregation from the bulk to the surface, the E_{seg-1}, E_{seg-2} and E_{seg-3} of Co atom are -0.53, 0.72 and -3.39 eV, respectively. Thus, the segregation of Fe atom is much easier than the segregation of Co atom in the presence of CO adsorption. Above results show that compared to the segregation of Fe or Co atom in the CoFe alloy in the absence of CO adsorption, CO adsorption promotes the segregation of Fe atom; while it suppresses the segregation of Co atom. As a result, under CO atmosphere, the presence of CO adsorption promotes the Fe atom segregation in the CoFe alloy instead of the Co atom segregation, and the CoFe alloy presents the enriched surface Fe atoms, which are preferentially carburized to form a Fe_xC shell on the CoFe alloy.

Aiming at further analyzing the preference of Fe or Co atom segregation in the CoFe alloy, the reaction energy of Fe or Co atom segregation pathway is calculated. As mentioned above, in general, the alloy segregation takes place with the exchanges between the metal ions and surface/subsurface vacancies[1-3]. Our results show that the formation energies of Fe or Co vacancy

initially set in the 2nd layer with the absence of CO adsorption are 5.5 or 2.0 eV, namely, the formation of Co vacancy in the 2nd layer for CoFe alloy more easily occurs compared to that of Fe vacancy. Further, compared to the CoFe alloy surface in the absence of CO adsorption, CO adsorption promotes the formation of Fe or Co vacancy in the 2nd layer for CoFe alloy, however, the formation energy of Co vacancy is lower than that of Fe vacancy (-16.0 vs. -14.3 eV), namely, the formation of Co vacancy is much easier than that of Fe vacancy. Above results show that the formation of Co vacancy for the CoFe alloy is easier than that of Fe vacancy irrespective of CO adsorption, thus, only the Co vacancy in the 2nd layer for CoFe alloy is considered in our study.

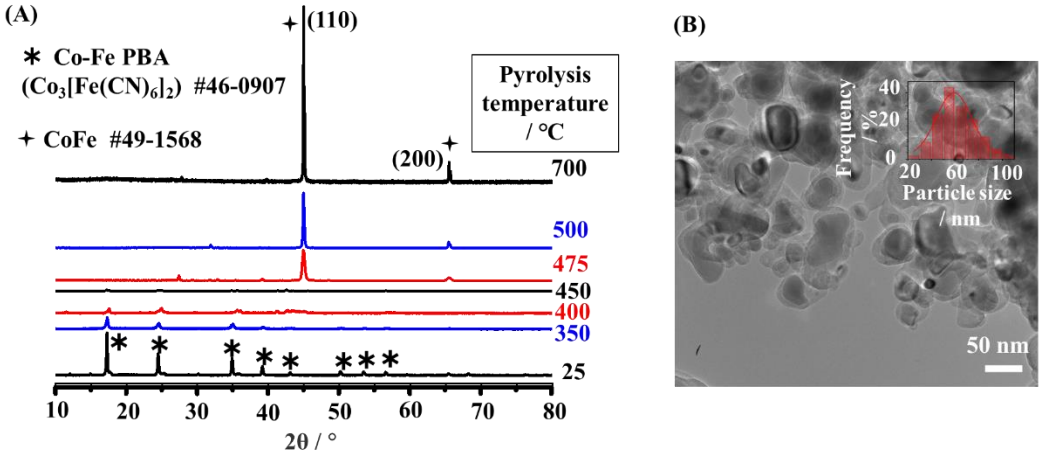

Figure S6 XRD patterns of Co-Fe PBA with various pyrolysis temperatures (A). The TEM image of the CoFe@C with the size distribution histogram (The iron size distribution is obtained from TEM images analysis by using at least 100 NPs.) (B).

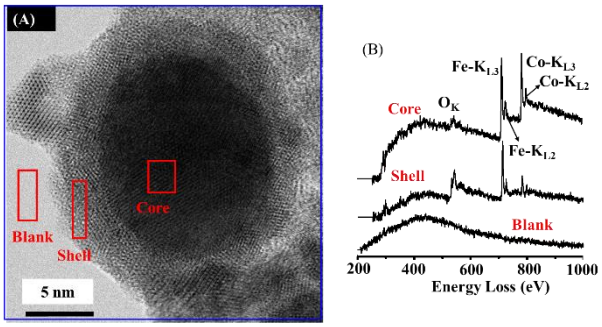

Figure S7 The STEM image (A) and EELS spectra from locations marked as core, shell and blank (B) of the CoFe@FeO_x.

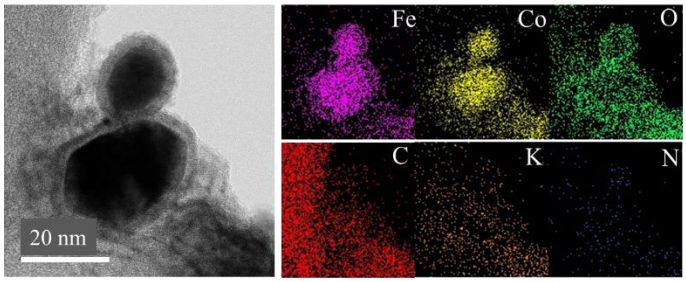

Figure S8 The STEM image and corresponding EDS elemental mapping images of the CoFe@FeO_x.

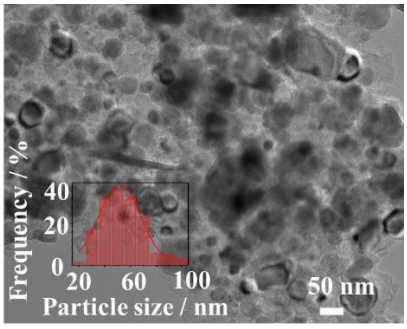

Figure S9 The TEM image of the CoFe@FeO_x with the size distribution histogram (The size distribution is obtained from TEM images analysis by using at least 100 NPs.).

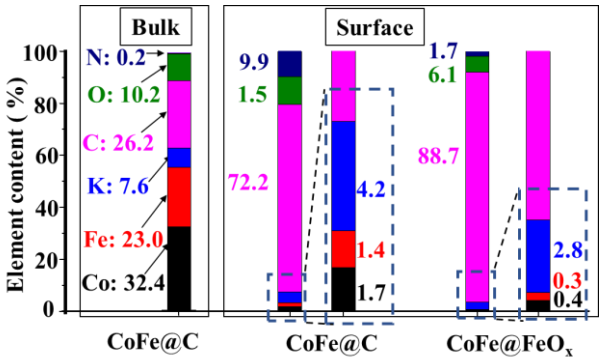

Figure S10 Element content of the bulk (obtained by ICP and element analyzer) and the surface (obtained by XPS) of the CoFe@C and CoFe@FeO_x.

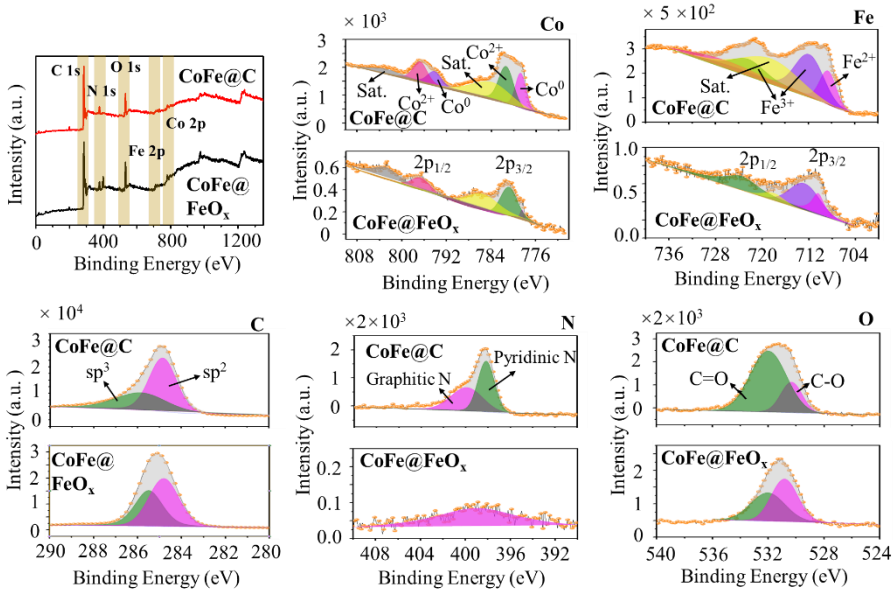

Figure S11 XPS files of the CoFe@C and CoFe@FeO_x.

Table S1 Mössbauer parameters of the CoFe@C and CoFe@FeO_x

Samples	Assignment	IS (mm s^{-1})	QS (mm s^{-1})	Bhf (T)	Area (%)
CoFe@C	CoFe alloy	0.011	0.00	34.0	96
	FeO_x	0.40	0.97	0.0	4
CoFe@FeO_x	CoFe alloy	0.012	0	34.19	72
	FeO_x	0.26	0.86	0	21
	Fe_xC	0.32	0	11.92	7

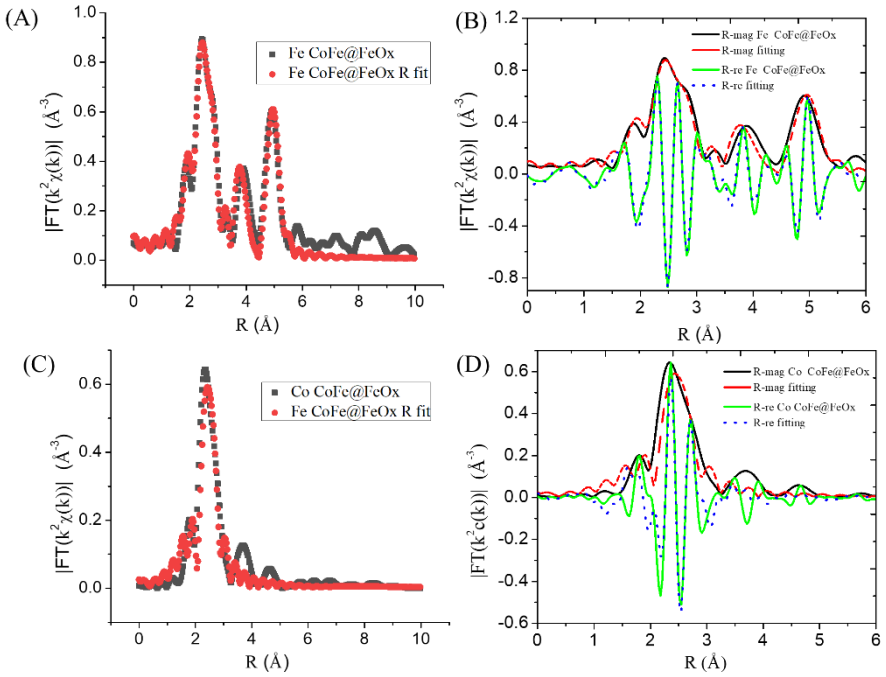

Figure S12 χ(R) space spectra fitting curve (A) and the inverse FT χ(R) space spectra into χ(q) space spectra (χ(k) space) fitting curve (B) of the CoFe@FeO_x at Fe K edge. χ(R) space spectra fitting curve (C) and the inverse FT χ(R) space spectra into χ(q) space spectra (χ(k) space) fitting curve (D) of the CoFe@FeO_x at Co K edge.

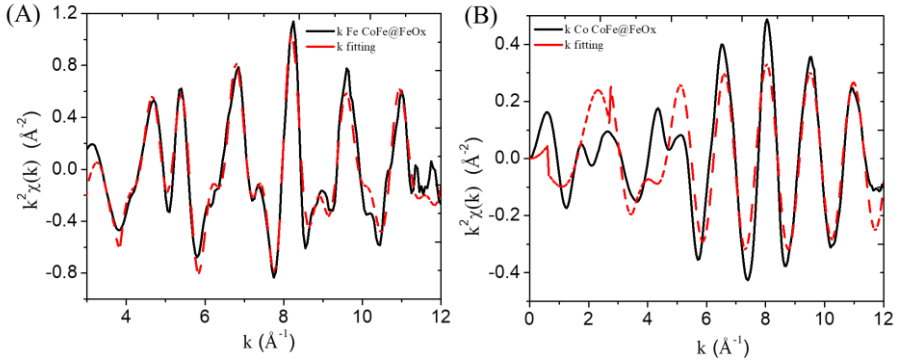

Figure S13 The experimental and fitted data of Fe (A) and Co (B) K-edge EXAFS of the CoFe@FeO_x.

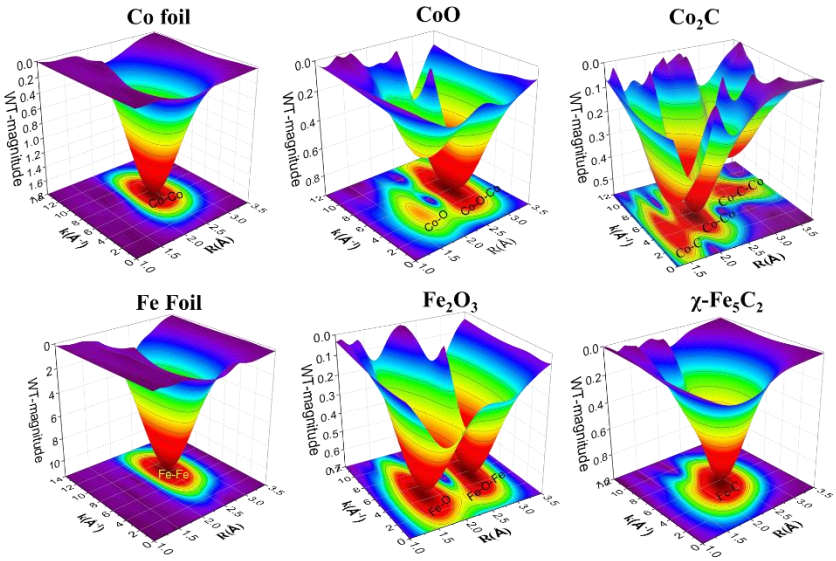

Figure S14 Co K edge WTEXAFS of reference Co foil, CoO, and Co_2C, and Fe K edge WTEXAFS of reference Fe foil, Fe_2O_3, and χ-Fe_5C_2.

Table S2 EXAFS best fitting parameters for Co and Fe K-edge data of the $CoFe@FeO_x$

Sample	Shell	N	R(Å)	ΔE_0 (eV)	σ^2 (Co-C path)	R-factor （%）
Co	Co-C	2	1.882 ± 0.059	4.49+/- 1.74	3.3+/-1.3	0.0592
	Co-Fe	3	2.368 ± 0.048	4.76+/-1.82	2.8+/-1.1	
Fe	Fe-O	2	1.909 ± 0.059	4.97+/- 1.63	5.5+/-2.3	0.0321
	Fe-C	3	2.283 ± 0.026	3.79+/-2.31	4.9+/-1.8	
	Fe-Co	2	2.589 ± 0.031	2.04+/-1.34	4.8+/-2.5	

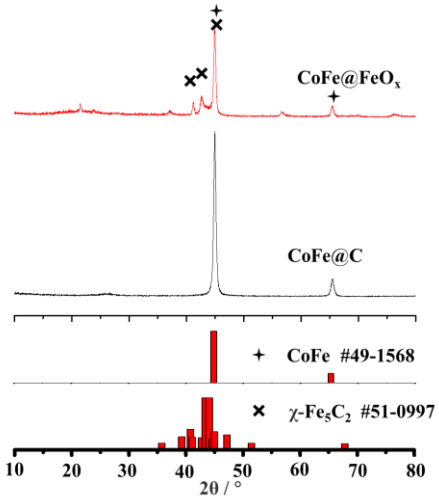

Figure S15 XRD patterns of the CoFe@C and $CoFe@FeO_x$.

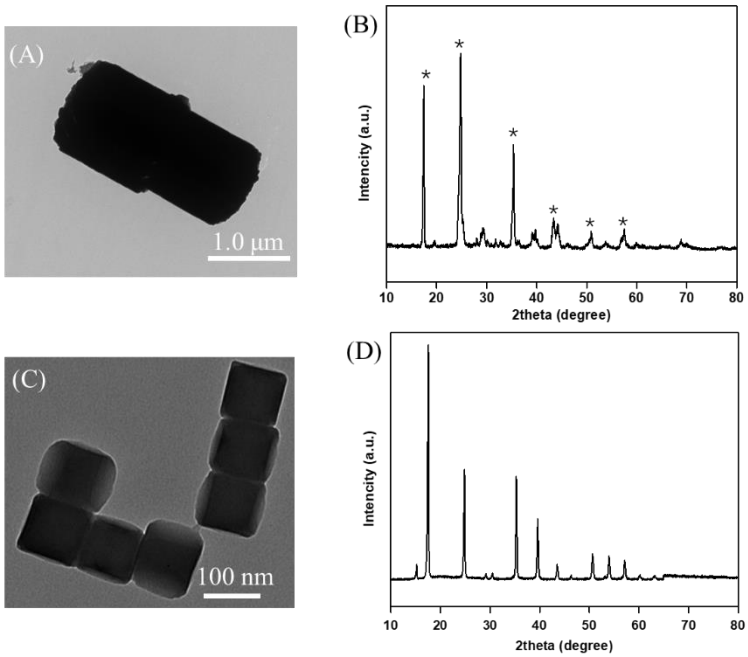

Figure S16 TEM image (A) and XRD patterns (B) of Mn-Fe PBA. TEM image (C) and XRD patterns (D) of Ni-Fe PBA.

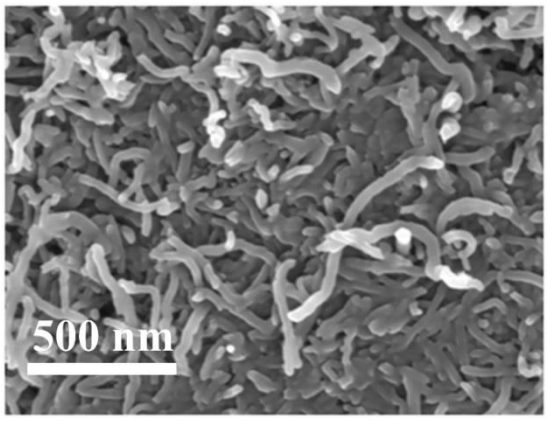

Figure S17 The commercial multiwalled CNTs and S powder composite cathode (S content: 70 wt%).

Commercial multiwalled CNTs and S powder composite is employed as cathode, in which active S accounts for 70 wt% in the composite cathode as shown in Figure S17.

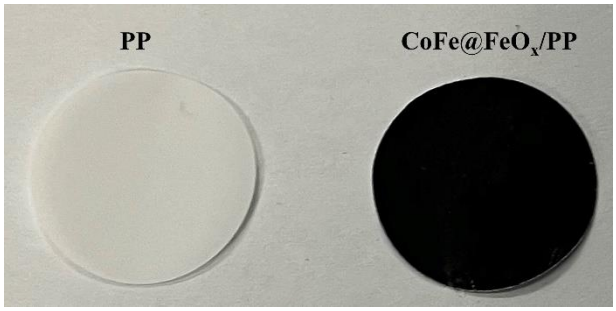

Figure S18 The optical photographs of the commercial PP separator and CoFe@FeO$_x$/PP separator.

The CoFe@FeO$_x$/PP obtained via the tape casting exhibits smooth surface according to the optical photographs in Figure S18, which is similar to that of commercial PP separator.

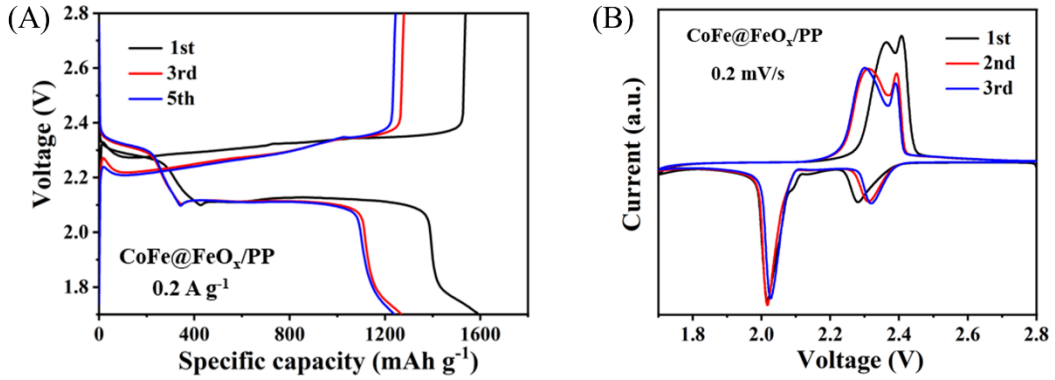

Figure S19 The typical charge/discharge curves at 0.2 A g^{-1} (A) and typical CV curves at 0.2 mV/s (B) of Li-S battery with CoFe@FeO$_x$/PP.

The charge/discharge curves of Li-S battery are shown in Figure S19A. The battery with CoFe@FeO$_x$/PP can deliver a high initial capacity of 1537 mAh g^{-1} (around 92% of theoretical value) at 0.2A g^{-1}. According to CV curves at 0.2 mV/s (Figure S19B), two typical cathodic peaks can be assigned to the sequential reduction of S_8 to soluble LiPSs and further convert to solid Li_2S_2/Li_2S. The charge plateau at 2.23-2.42 V is related to oxidation reaction of Li_2S to LiPSs and S_8.

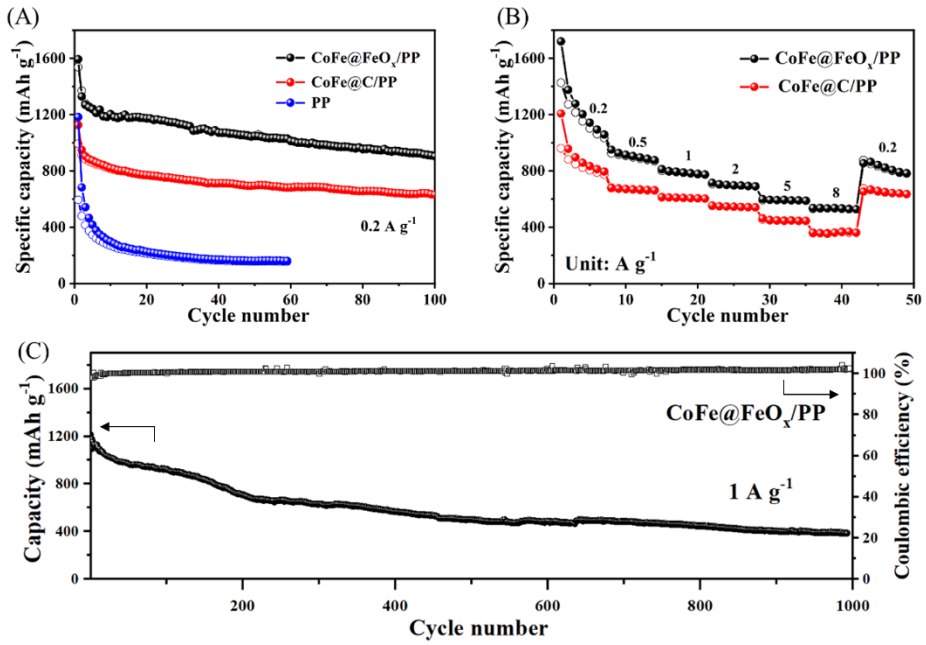

Figure S20 Cycling performance comparison of Li-S batteries with different separators at 0.2 A g^{-1} (A). Rate capability comparison of CoFe@FeO_x/PP and CoFe@C/PP based Li-S batteries at various current densities (B). Long-term cycling life of CoFe@FeO_x/PP based Li-S batteries at 1 A g^{-1} (C).

Detailed performance comparisons of Li-S batteries with traditional PP separator, CoFe@C/PP and CoFe@FeO_x/PP are exhibited in Figure S20A. The Li-S battery with CoFe@FeO_x/PP can maintain a high reversible capacity of 913 mAh g^{-1} after 100 cycles. As a contrast, a low initial capacity of 595 mAh g^{-1} is obtained with the traditional PP separator, demonstrating the CoFe@FeO_x can effectively anchor LIPSs and facilitate the conversion of sulfur species. And the Li-S battery with the CoFe@C/PP exhibits an initial reversible capacity of 993 mAh g^{-1} at 0.2 A g^{-1} and maintain a high capacity of 631 mAh g^{-1} after 100 cycles, which is poorer than that of the CoFe@FeO_x based battery. The rate performance comparison of batteries with the CoFe@FeO_x/PP and CoFe@C/PP are showed in Figure S20B. The CoFe@FeO_x based battery can exhibit high specific capacities of 1376, 927, 799, 706, 594 and 536 mAh g^{-1} at 0.2, 0.5, 1, 2, 5 and 8 A g^{-1}, respectively. However, the battery with CoFe@C/PP could only deliver specific capacities of 957, 675, 612, 549, 451 and 358 mAh g^{-1} at 0.2, 0.5, 1, 2, 5 and 8 A g^{-1}, respectively. The long-term cycling performance with the CoFe@FeO_x/PP is evaluated at 1 A g^{-1} as shown in Figure S20C, which could deliver a long lifespan around 1000 cycles. The superior electrochemical performance suggests that the CoFe@FeO_x with abundant polar active sites in the FeO_x shell and highly conductive CoFe alloy core can significantly suppress the shuttling of polysulfides and promote the conversion process of LIPSs.

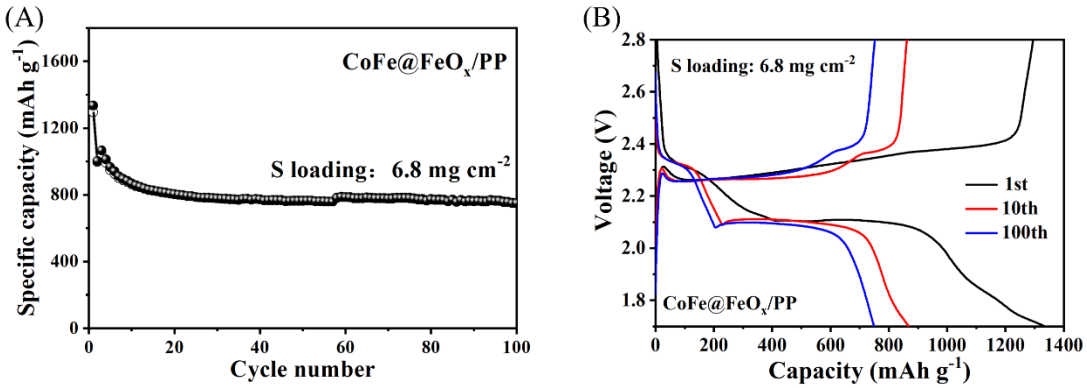

Figure S21 Cycling performance (A) and corresponding charge/discharge curves (B) of CoFe@FeO_x/PP based battery with high sulfur loading of 6.8 mg cm^{-2} at 0.1 A g^{-1}.

The high areal S loading electrode is fabricated to further check practical application of Li-S batteries with the CoFe@FeO_x/PP (Figure S21). Even with high sulfur loading mass of 6.8 mg cm^{-2}, the CoFe@FeO_x based battery can achieve a high initial capacity of 1294 mAh g^{-1} and maintain a superior reversible capacity of 752 mAh g^{-1} after 100 cycles at 0.1A g^{-1}, indicating the desirable application prospect of CoFe@FeO_x for boosting high energy density practical Li-S batteries.

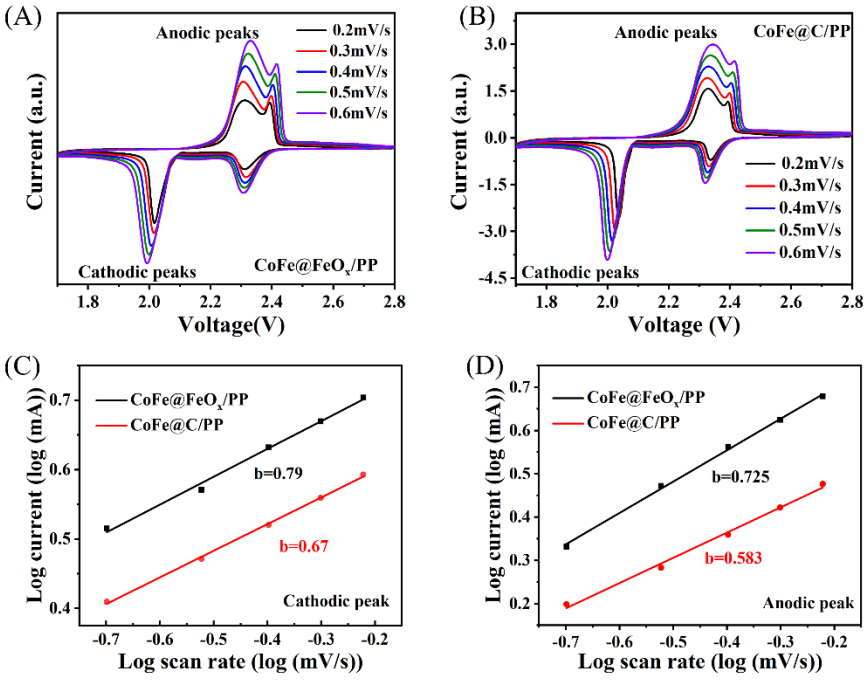

Figure S22 CV curves of CoFe@FeO_x/PP (A) and CoFe@C/PP (B) based Li-S batteries at various scan rates. The linear fitting plots of CoFe@Fe_3O_4/PP and CoFe@C/PP based batteries (C, D).

The reaction dynamics comparisons between the CoFe@FeO_x and CoFe@C based batteries are analyzed via the power-law equation (log(i) = log(a) + blog(v), i and v are the peak current and scanning rate and a and b are the adjustable parameters).[23] *Both the cathodic peak and anodic peak with the CoFe@FeO_x based battery show higher b values than those of the CoFe@C based battery, demonstrating much faster reaction kinetics with the CoFe@FeO_x/PP.*

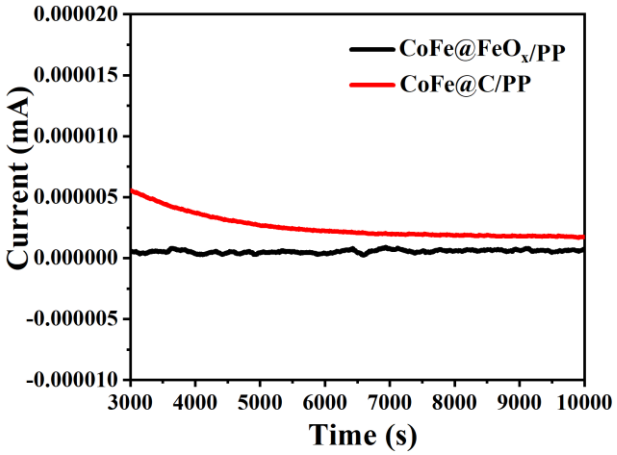

Figure S23 The shuttle current measurement for Li-S batteries with CoFe@FeO_x/PP and CoFe@C/PP.

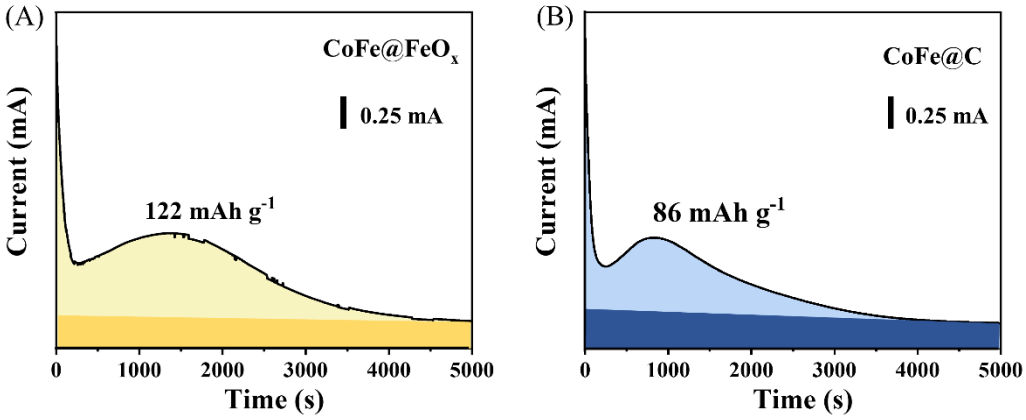

Figure S24 The Li_2S precipitate experiments for Li-S batteries with CoFe@FeO_x and CoFe@C.

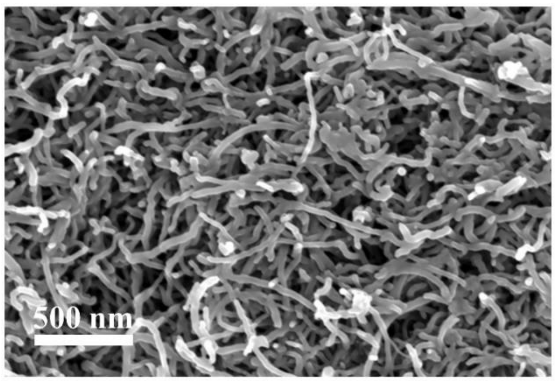

Figure S25 The commercial multiwalled CNTs and S powder composite cathode (S content: 50 wt%).

In view of more slower reaction kinetics derived from larger Na ion radius and more severe volume expansion issues of Na-S batteries than those of Li-S batteries, the CNTs and S composite cathode with S content of 50 wt% is attempted to assemble RT Na-S batteries. The CNTs and S composite cathode with good dispersion is shown in Figure S25.

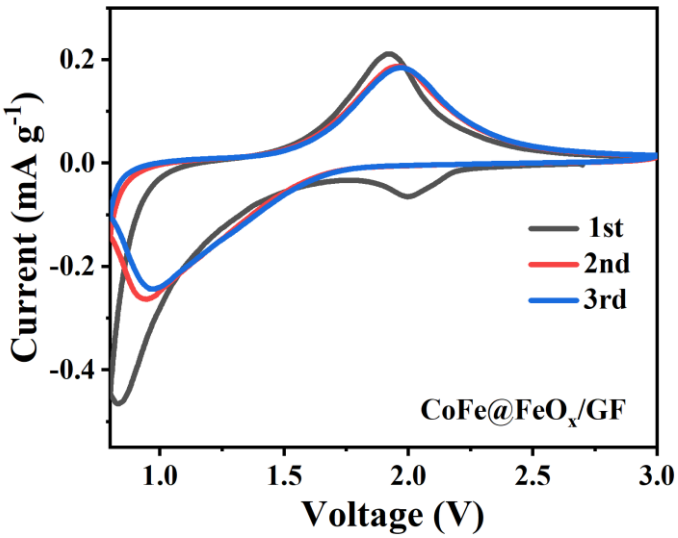

Figure S26 The typical CV curves of RT Na-S battery with CoFe@FeO_x/GF at 0.2 mV s^{-1}.

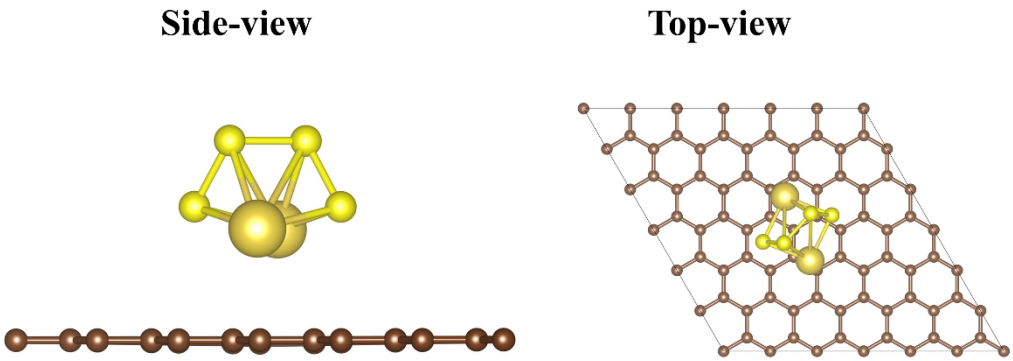

Figure S27 Optimized adsorption configuration of Na_2S_4 on the surface of graphite.

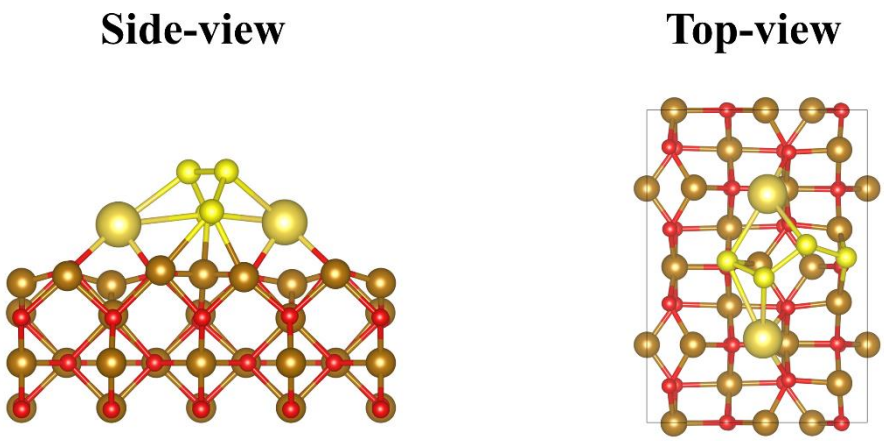

Figure S28 Optimized adsorption configuration of Na_2S_4 on the surface of Fe_3O_4.

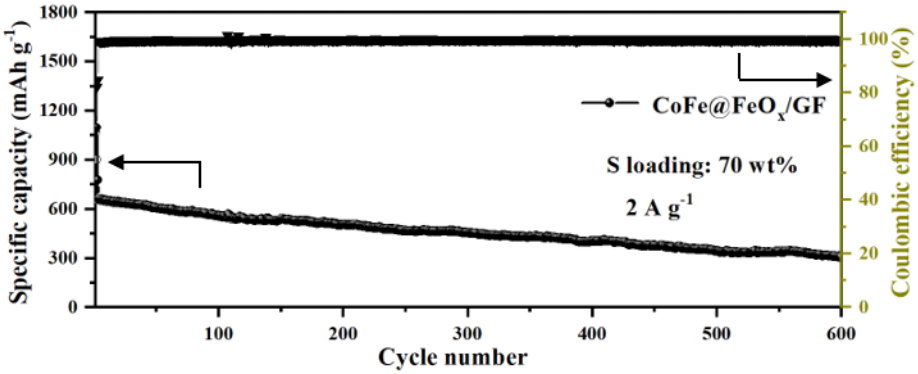

Figure S29 Cycling performance of CoFe@FeO_x/GF separator based RT Na-S batteries at 2 A g^{-1} with high sulfur content of 70 wt%.

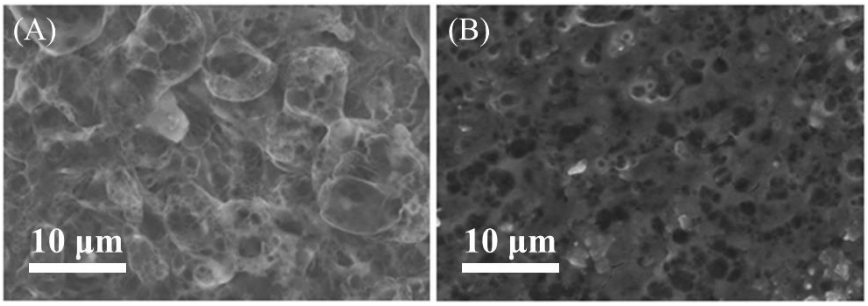

Figure S30 The morphologies of Na anode for RT Na-S batteries with commercial GF separator (A) and CoFe@FeO_x/GF separator (B) after three cycles at 0.2 A g^{-1}.

The morphologies of Na anode with commercial GF separator and CoFe@FeO_x/GF after three cycles at 0.2 A g^{-1} are displayed in Figure S30. Na anode exhibits rough and corroded surface in RT Na-S battery with the commercial GF separator. When used the CoFe@FeO_x/GF separator, the Na anode presents relatively smooth surface, further demonstrating the CoFe@FeO_x/GF separator could inhibit the shuttle effect and protect the Na anode.

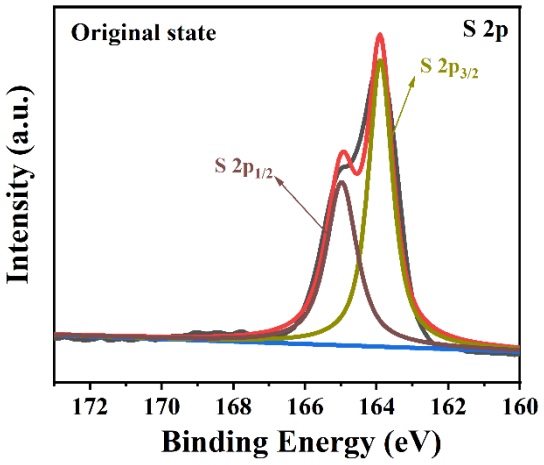

Figure S31 Ex situ XPS spectra of the CoFe@FeO_x/GF based RT Na-S battery measured at original state.

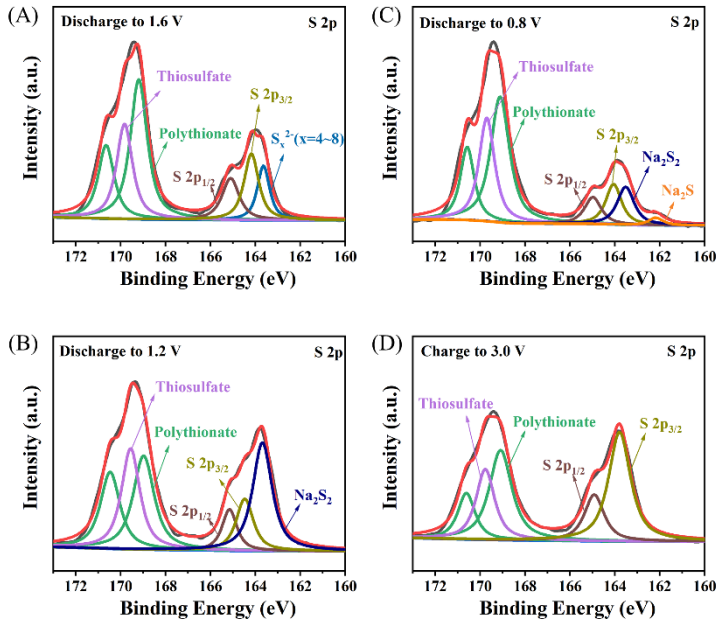

Figure S32 Ex situ XPS spectra of the CoFe@Fe_3O_4/GF based RT Na-S batteries measured at different discharge/charge states: Discharge to 1.6 V (A), discharge to 1.2 V (B), discharge to 0.8 V (C) and charge to 3.0 V (D).

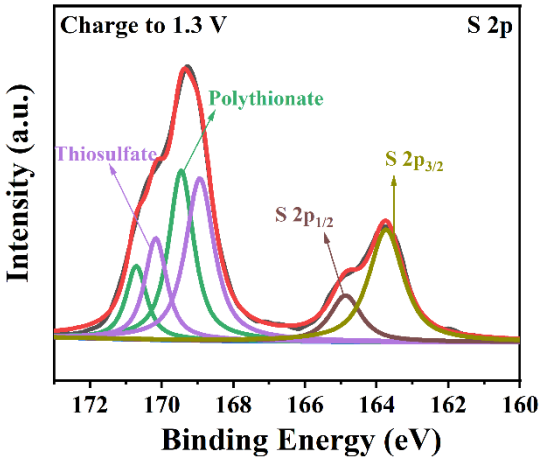

Figure S33 Ex situ XPS spectra of the CoFe@FeO_x/GF based RT Na-S battery measured at the charge state of 1.3 V.

References

1. Zhang, X. et al. Reversible loss of core–shell structure for Ni–Au bimetallic nanoparticles during CO_2 hydrogenation. *Nat. Catal.* **2020,** *3*, 411-417.
2. Kim, H. et al. CO Adsorption-driven surface segregation of Pd on Au/Pd bimetallic surfaces: Role of defects and effect on CO oxidation. *ACS Catal.* **2013,** *3*, 2541-2546.
3. An, H. et al. Understanding the atomic-level process of CO-adsorption-driven surface segregation of Pd in $(AuPd)_{147}$ bimetallic nanoparticles. *Nanoscale* **2017,** *9*, 12077-12086.